

# Tailoring Carbon Microcrystals for Ultrafast Lithium Storage

Feifei Mao, Xiangyang Kong, Shasha Gao,\* Penggao Liu, Yong-Zheng Fang,\* and Zhen Zhou

The demand for high energy density, fastcharging capability, and extended working life is crucial for next-generation lithium-ion batteries (LIBs) employed in consumer-grade electronic devices and electric vehicles. However, the presently utilized graphite anode exhibits sluggish ion kinetics and limited specific capacity owing to its fixed crystal structure and restricted interlayer distance. Herein, a large-size cation shear strategy for regulating carbon crystals is demonstrated. During the carbonization process, the shuttling of cations within the carbon skeleton inhibits the horizontal growth and longitudinal stacking of the carbon crystals, thereby successfully synthesizing ultramicrocrystalline carbon with short-range order and abundant microporous

structures. As a result of the optimized carbon lattices, Li-ion insertion mechanism and dynamics are greatly improved, exhibiting a super high Li-storage capacity of  $1156 \text{ mAh g}^{-1}$  at  $0.1 \text{ A g}^{-1}$  (three times that of graphite theoretical capacity) and excellent rate capability with  $375 \text{ mAh g}^{-1}$  maintained at  $6 \text{ A g}^{-1}$  (100% graphite theoretical capacity). The assembled  $\text{LiNi}_0.6\text{Co}_{0.2}\text{Mn}_{0.2}$ -based full batteries achieve excellent fast charging capability and long cycle stability, with a 92% energy retention rate after 500 cycles. This carbon crystal regulation strategy demonstrates great potential for developing advanced carbon-based LIBs with high power and high energy.

## 1. Introduction

Lithium-ion batteries (LIBs) have garnered significant interest for energy storage and conversion compared to other energy storage systems due to their advancement, including elevated operating voltage, high specific energy, and long cycle life.<sup>[1,2]</sup> Nevertheless, the accelerating evolution of renewable energy infrastructures and electric mobility systems demands greater improvements in LIBs performance, particularly regarding energy and power densities.<sup>[3–6]</sup> Among the components of LIBs, anode

materials play a crucial role in their electrochemical performance.<sup>[7]</sup> Currently, graphite has been widely adopted as the primary anode material for commercial LIBs due to its reversible intercalation storage mechanism and accessibility.<sup>[8,9]</sup> However, its regular carbon crystalline structure imposes fundamental limitations.<sup>[10]</sup> Tightly oriented carbon stacking along the c-axis restricts Li-ion insertion, slowing bulk diffusion and limiting capacity to  $372 \text{ mAh g}^{-1}$ .<sup>[11]</sup> These seriously hinder the energy density and power density of LIBs using graphite anodes.

To improve the Li-ion storage performance in carbon, microstructure engineering plays a crucial role. Amorphous carbon outperforms graphite due to its abundant active sites, structural anisotropy, and expanded interlayer spacing, despite having only short-range order.<sup>[12]</sup> Hard carbon is a representative amorphous carbon composed of a turbulent graphitic lattice and large holes (1.5–2 nm).<sup>[13,14]</sup> The selection of hard carbon precursors largely determines their electrochemical performance. Ideal precursors should exhibit high carbon yield and controllable microstructure. Currently, the most common types include biomass-derived precursors and synthetic polymer precursors, among others.<sup>[15–17]</sup> This disordered architecture effectively inhibits graphitization while creating more Li-ion adsorption sites, thus delivering a higher Li storage capacity of  $400–700 \text{ mAh g}^{-1}$  at  $0.1 \text{ A g}^{-1}$  within  $0.01–1.5 \text{ V}$  (vs.  $\text{Li}^+/\text{Li}$ ).<sup>[18,19]</sup> Nevertheless, its unstable macroporous structure frequently induces lattice collapse or deformation during prolonged cycling, resulting in an unstable cyclic performance and low Coulombic efficiency (CE). Furthermore, the synthesis precursors typically contain large organic molecules with cross-linked structures, such as petroleum bitumen, resins, polymers, and biomass.<sup>[20,21]</sup> This results in low carbonization yield and high production costs. Hard carbon suffers from

F. Mao  
Longmen Laboratory  
Luoyang, Henan 471023, China

F. Mao, S. Gao  
Key Laboratory of Microelectronics and Energy of Henan Province  
Xinyang Normal University  
Xinyang 464000, China  
E-mail: gaoshasha0805@163.com

X. Kong, S. Gao, Y.-Z. Fang, Z. Zhou  
Interdisciplinary Research Center for Sustainable Energy Science and Engineering (IRCSE<sup>2</sup>)  
School of Chemical Engineering  
Zhengzhou University  
Zhengzhou, Henan 450001, China  
E-mail: yongzheng\_fang@zzu.edu.cn

P. Liu  
State Key Laboratory of Chemistry and Utilization of Carbon Based Energy Resources  
College of Chemistry  
Xinjiang University  
Urumqi 830017, China

 Supporting information for this article is available on the WWW under <https://doi.org/10.1002/batt.202500370>

unpredictable performance due to inherent material heterogeneity and random crystallization. In contrast, soft carbon, another amorphous structure with graphitization potential, presents a relatively continuous yet loose lattice arrangement.<sup>[22]</sup> Such a structure enables rapid Li-ion diffusion kinetics through the graphitic lattice, thereby enhancing rate capability. In addition, soft carbon synthesis primarily utilizes high-carbon-content precursors, which endow it with favorable consistency and cost advantages.<sup>[23]</sup> However, the thermal carbonization process will gradually induce its graphitization evolution, accompanied by micropore collapse, leading to a reduction in active sites and limited capacity ( $200\text{--}500\text{ mAh g}^{-1}$ ).<sup>[24,25]</sup> Conversely, inadequate graphitization results in crystal instability and poor electrochemical reversibility.<sup>[26]</sup> In short, these common carbon crystalline architectures universally exhibit inherent limitations and mutually exclusive advantages. This is a significant challenge in effectively integrating their respective advantages through rational structure engineering to prepare an ideal carbon architecture. That should maintain a certain carbonization degree to ensure electrochemical activity while suppressing excessive graphitization degree to improve Li-ion diffusion kinetics.<sup>[27]</sup> Simultaneously, it requires a stable micropore yet non-hard carbon macroporous structure to increase Li storage capacity and ensure structural stability.

Herein, we propose a cation perturbation strategy to achieve effective regulation of carbon crystals. By employing various cationic molten salts as the carbon layer shear agents and activators during the high-temperature carbonization process, we demonstrate that large-sized cations can modulate the crystal structure of carbon materials by shuttling within the carbon skeleton, mainly through creating pores and promoting microcrystalline evolution. The introduction of molten salt offers distinct advantages for the preparation of microcrystalline porous carbon. Specifically, the molten salt effectively reduces the crystallization

temperature of soft carbon, eliminating the need for high-temperature graphitization and thereby significantly lowering energy consumption. Particularly, the  $\text{ZnCl}_2/\text{KCl}$  mixed salt drives the formation of ultracrystalline carbon that effectively inhibits the graphitization process, and exhibits numerous short-range ordered microcrystalline textures and micropore structure. Such microcrystall/micropore configuration generates abundant edge-defect active sites and ultrashort ions diffusion channels, thereby exhibiting a remarkable reversible capacity ( $1156\text{ mAh g}^{-1}, 0.1\text{ A g}^{-1}$ ) and superior rate capability ( $375\text{ mAh g}^{-1}, 6\text{ A g}^{-1}$ ). When used as anodes for NCM full batteries, the full battery achieves a high energy density of  $275\text{ Wh kg}^{-1}$  and high power density of  $633\text{ W kg}^{-1}$ , as well as outstanding cycling performance with 92% energy retention after 500 cycles. These findings demonstrate the effectiveness of the carbon crystal regulation strategy for high-performance LIBs.

## 2. Results and Discussion

Compared to graphite carbon with highly ordered crystalline structures and hard carbon containing excessive macropore defects, soft carbon presents moderately adjustable lattice configurability. Blind coal emerges as a desired precursor for soft carbon synthesis due to its abundant availability and high carbon content (>90%).<sup>[28]</sup> To obtain porous architectures and mitigate graphitization during the coal carbonization process, we employed three chloride salts with distinct cationic species, including  $\text{LiCl}$ ,  $\text{ZnCl}_2$ , and  $\text{KCl}$ , as the activators and pore-forming agents for carbon. As shown in Figure 1, the pretreated blind coal, after being pulverized and acid-washed, was dispersed in the high-temperature ionic liquid solvent and subsequently carbonized. During this process, the little organic components and impurities in the coal will be removed, and the cations can inhibit

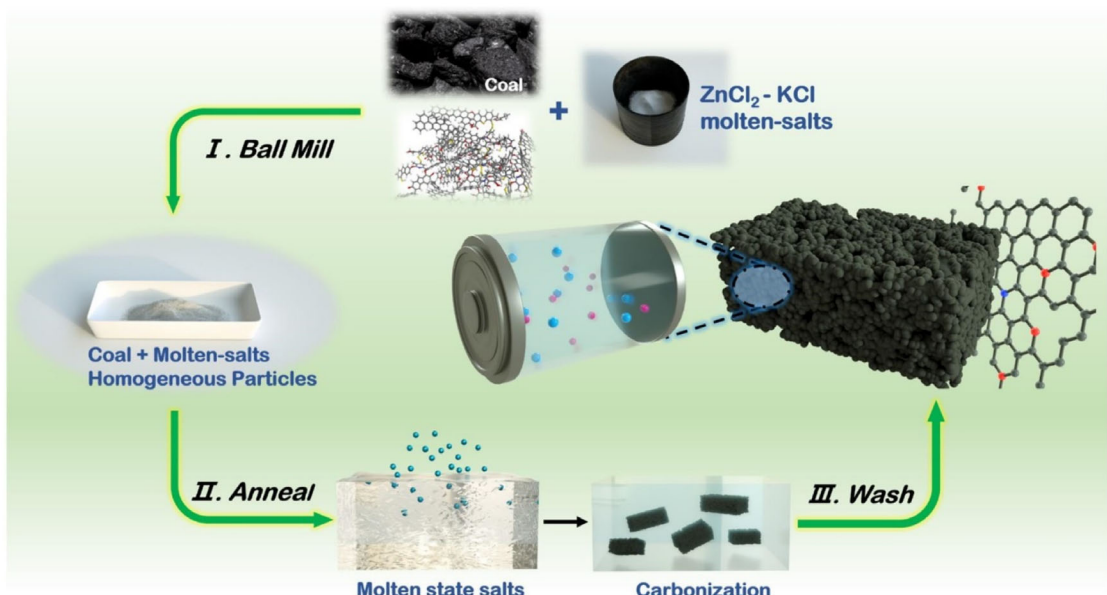


Figure 1. Schematic of the crystalline carbon preparation process.

the growth and compact aggregation of carbon microcrystals, resulting in the formation of a unique porous microcrystal carbon structure. The synthesized coal carbon (CC) using molten salt is designated as CC-X (X represents the cation in the used molten salt).

The microstructure of carbon materials is significantly affected by the type of molten salt and the calcination temperature. As observed by transmission electron microscopy (TEM, Figure 2), where blue, red, and black represent amorphous regions, crystalline regions, and pores, respectively. With temperature increasing from 600 to 1400 °C, the CC prepared without any molten salts displays a gradual increase in the red regions with long lattice fringes occurring (>2 nm), confirming the concurrent progression of the carbonization and graphitization processes as the temperature increases (Figure 2a,b, S1, Supporting Information). Notably, when adding the LiCl and KCl, the synthesized CC-Li and CC-Li/K present a significant increase in the amorphous and micropore regions, as evidenced by the expanded blue and black areas, respectively (Figure 2c,d, S2, S3, Supporting Information), compared to the CC across different calcination temperatures. This demonstrates that the shuttling of the introduced cations within the carbon skeleton can effectively inhibit the carbonization and graphitization process, even at the higher temperature (1400 °C, Figure S2c, S3c, Supporting Information). Additionally, compared to LiCl salt, the incorporation of KCl further promotes an increase in both the number and size of micropores within carbon

skeletons, which may be attributed to the larger ionic radius of  $K^+$  relative to  $Li^+$ , revealing a significant pore-forming capability of KCl. Nevertheless, a large number of amorphous regions (blue) are not conducive to reversible Li storage.

Fortunately, we found that  $ZnCl_2$  molten salt could significantly promote carbon crystallization. As shown in Figure 2e and S4, Supporting Information, the CC-Zn synthesized using  $ZnCl_2$  salt exhibits a significantly expanded crystalline region (red) compared to CC-Li and CC-Li/K, and even the CC. This confirms the effectiveness of Zn-ions in reducing the crystallization energy barrier of carbon. Structural comparisons further reveal that CC-Zn presents a distinct microcrystalline architecture with shorter and more distorted lattice fringes, which is obviously different from the graphitization textures evolution observed in the CC during the carbonization process. The results demonstrate that Zn-ions simultaneously accelerate carbonization kinetics while suppressing long-range crystalline ordering, revealing an inhibited graphitization process. Such a microcrystalline structure is conducive to promoting  $Li^+$  bulk diffusion, but it is ineffective in enhancing the Li storage capacity. To further create more Li storage sites, the KCl molten salt was collaboratively employed. As shown in Figure 2f, the CC-Zn/K synthesized using  $ZnCl_2/KCl$  salts achieves both microcrystalline and microporous characteristics, which is attributed to the synergistic effect of Zn-ion promoting crystallization and K-ion inducing pore formation. Such cation-driven structural modifications remain effective under different

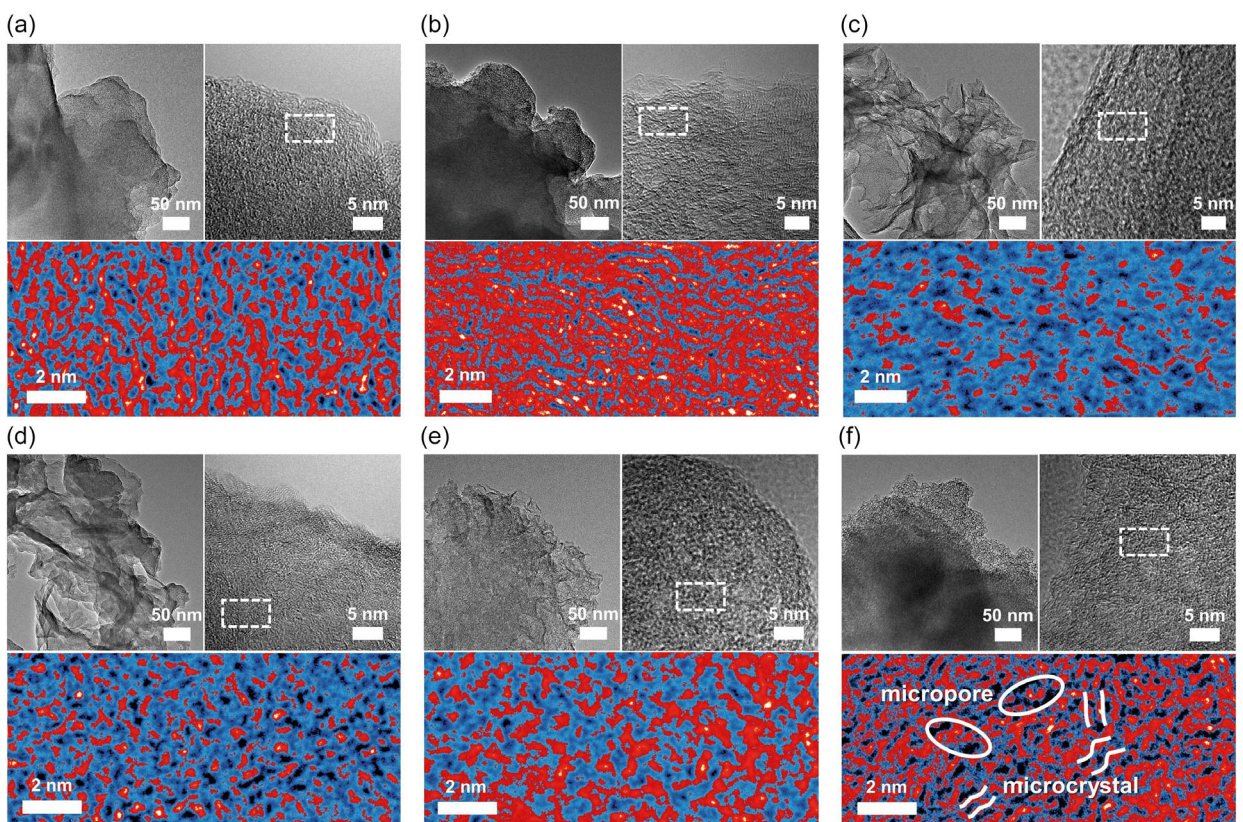


**Figure 2.** Microscopic morphology comparison of CC and CC-Xs. TEM and High-Resolution Transmission Electron Microscope images of a) CC-800 °C, b) CC-1400 °C, c) CC-Li-800 °C, d) CC-Li/K-800 °C, e) CC-Zn-800 °C, and f) CC-Zn/K-800 °C.

calcination temperatures (Figure S5, Supporting Information), again confirming the graphitization inhibition effect. These results emphasize that cations in the molten salt have a significant regulatory effect on the carbon crystal growth and the generation of defects during the carbonization process.

To investigate the influence of cationic salts on crystal structure, these carbons were synthesized using different cationic molten salts at 800 °C and were further examined. As shown in X-ray diffraction (XRD) patterns (Figure 3a), the broad characteristic peaks at 26.6° and 43° can be attributed to the (002) and (100) crystalline facets of carbon.<sup>[23]</sup> Compared to the pure CC, the CC-X synthesized using cationic molten salts all exhibit smaller (002) peak intensity and wider peak shape, confirming a lower graphitization degree due to the shuttling of cations within the carbon skeleton, especially when using molten salts containing K-ions with pore-forming effect. Furthermore, the CC-Zn and CC-Zn/K present significantly shifted (002) diffraction peaks toward lower angles, suggesting the microcrystalline structure induced by Zn-ions possesses a larger interlayer distance.<sup>[29]</sup> This will be conducive to the Li<sup>+</sup> diffusion between interlayers.

The Raman spectra test was conducted to further analyze the graphitization degree of these carbons (Figure 3b). The characteristic peaks observed at 1350 and 1580 cm<sup>-1</sup> are defined as the D and G peaks of carbon, which correspond to the vibrations of the sp<sup>3</sup> and sp<sup>2</sup> carbon atoms within the disordered regions of the hexagonal graphite layer, respectively.<sup>[30]</sup> The obvious D peaks observed in CC-X confirm the presence of disordered microcrystals or defects. The I<sub>D</sub>/I<sub>G</sub> values, signifying the level of disorder,<sup>[31]</sup> are calculated to 0.911, 0.969, 0.986, 0.953, and 0.963, for CC, CC-Li, CC-Li/K, CC-Zn, and CC-Zn/K, respectively (Figure 3c). This Raman result further confirms that Li-ions, K-ions, and Zn-ions can effectively inhibit graphitization of carbon materials.

Especially, the addition of K ions demonstrates a stronger influence on inducing carbon defects, which is attributed to their pore-forming effect.

The pore structure and specific surface area were investigated through the N<sub>2</sub> adsorption-desorption test. As shown in Figure 3d, the cation-driven CC-Xs present a rapid increase in N<sub>2</sub> adsorption at relatively low pressures, indicating the presence of abundant micropores in the samples. According to the

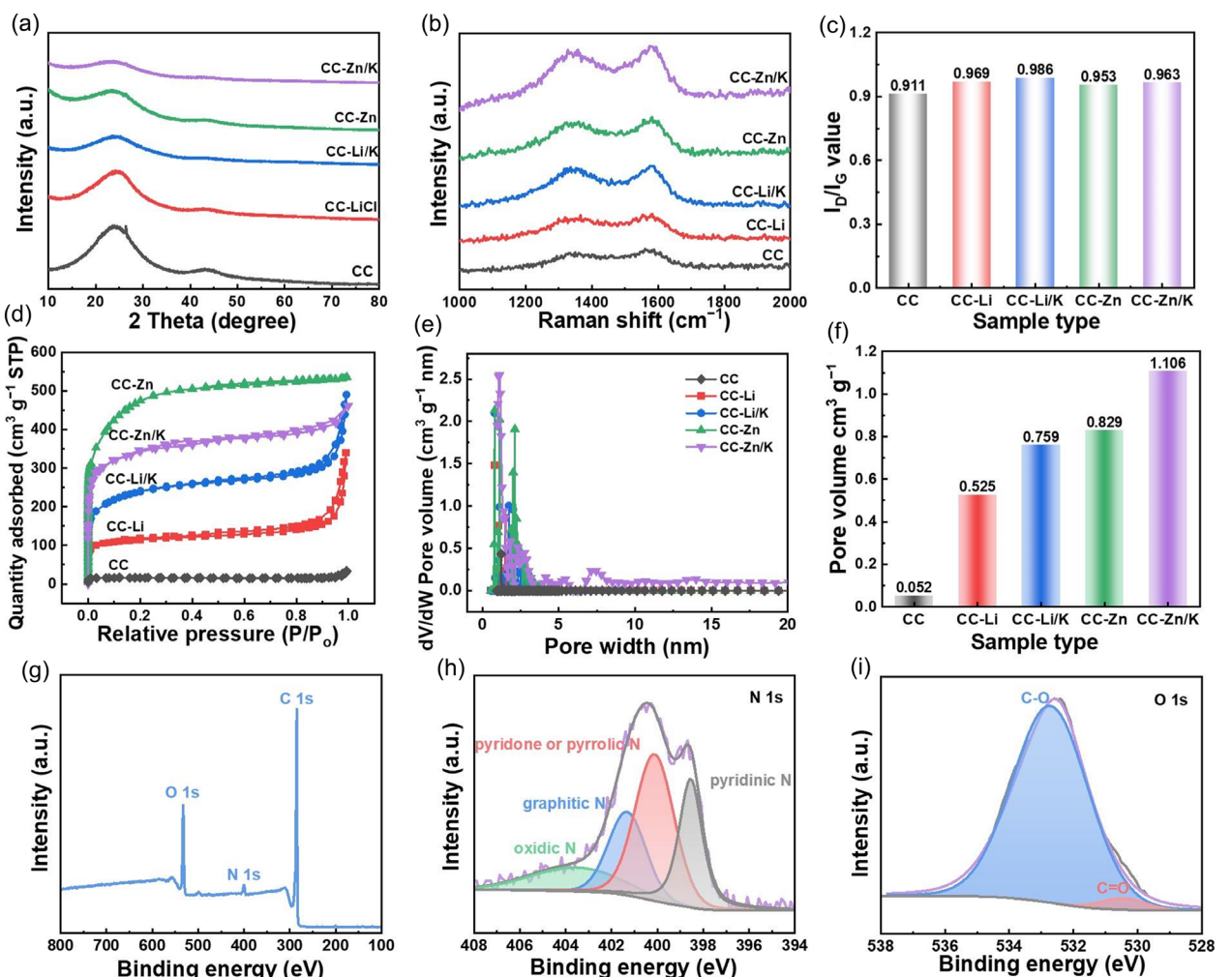


**Figure 3.** Comparison of carbon structures of CC and CC-Xs. a) XRD patterns; b) Raman spectra; c)  $I_D/I_G$  values; d) N<sub>2</sub> adsorption–desorption isotherms; e) pore size distribution profiles and f) pore volume calculation; g) XPS survey spectra, and high-resolution spectra of h) N 1s and i) O 1s of CC-Zn/K.

adsorption–desorption curves, the specific surface area of the CC, CC-Li, CC-Li/K, CC-Zn, and CC-Zn/K is calculated to be 44, 765, 1529, 357, and  $1274 \text{ m}^2 \text{ g}^{-1}$ , respectively. This demonstrates that the cations shuttling within the carbon skeleton lead to a significant increase in specific surface area due to the formation of more microporous structures, especially K-ions-driven CC-Li/K and CC-Zn/K. To further analyze the pore structure, the pore size distribution was investigated, demonstrating that the shuttling of cations within the carbon skeleton mainly induces the formation of microporous structures ( $<2 \text{ nm}$ , Figure 3e). According to the calculation in Figure 3f, the CC-Xs all exhibit a significant increase in pore volume than the unmodified CC, confirming the effectiveness of cationic salts for the pore formation. Notably, the CC-Zn/K exhibits maximal pore volume ( $1.106 \text{ cm}^3 \text{ g}^{-1}$ ) compared with other CC-Xs, which implies that the microcrystalline and microporous structures have a synergistic promoting effect that the formation of microcrystals is conducive to preventing the micropores closure during the carbonization process.

The surface elements of the CC-Zn/K were detected by energy-dispersive spectroscopy (EDS) and X-ray photoelectron spectroscopy (XPS) tests. As the EDS mapping shows (Figure S6, Supporting Information), the CC-Zn/K exhibits a predominant presence of C, with a few N and O elements on the surface. The doping elements can be attributed to the decomposition of organic components in coal, which is beneficial in increasing the active reaction sites. The surface elements content was further analyzed using XPS, again verifying the presence of N and O (Figure 3g), with 3.7% and 15.8% surface proportion, respectively (Figure S7, Supporting Information). The relatively high N and O content could be attributed to the existence of substantial micropores and microcrystals that retain O and N groups on the edges of carbon defects. Their bonding mode is further analyzed in high-resolution XPS spectra. N-spectrum exhibits four peaks at around 398.5, 400.1, 401.3, and 403.5 eV, representing pyridinic N, pyrrolic N, graphitic N, and oxidized N, respectively (Figure 3h).<sup>[32]</sup> The presence of pyridinic N and pyrrolic N contributes to enhancing the pseudocapacitance through reversible faradaic redox reactions in the electrochemical process. Meanwhile, the existence of graphitic N and oxidized N can increase the wettability and conductivity of the carbon materials.<sup>[33]</sup> Additionally, the O-spectrum displays the presence of C=O (531.6 eV) and C—O (533.0 eV, Figure 3h),<sup>[34]</sup> which can further improve the wettability and pseudocapacitance.<sup>[25]</sup> These abundant groups on the micropore edges fundamentally enhance the storage Li performance of microcrystalline carbon.

To further investigate the influence of microcrystalline and microporous structures on Li storage performance, half-cells were assembled using carbon with different structures as the work electrode and Li metal as the counter electrode. The initial cyclic voltammetry (CV) curves of CC-Zn/K tested at  $0.1 \text{ mV s}^{-1}$  exhibit an irreversible reduction peak below 1.0 V during the first discharge (Figure 4a), which is attributed to the formation of the solid–electrolyte interphase (SEI) film. Simultaneously, the initial charge–discharge curves and initial CE of graphite, CC, and CC-Zn/K were tested (Figure S8, Supporting Information). Graphite

exhibited the highest first-cycle reversibility (87.75%), while the surface doping present in CC-Zn/K during its preparation made the SEI formation process more complex, leading to a low CE of 62.60%. After that, the CV curves present a nearly unchanged rectangle-like shape in the subsequent cycles, indicating a reversible pseudocapacitive reaction process. The rate performance of the CC-Zn/K was further tested under different current densities, taking graphite, CC, and other CC-Xs as the comparison. As shown in Figure 4b, the CC-Zn/K exhibits high specific capacities of 1156, 884.7, 717.7, and  $520.8 \text{ mAh g}^{-1}$  at 0.1, 0.5, 1.0, and  $3.0 \text{ A g}^{-1}$ , respectively. Notably, even at a relatively high current density of  $6 \text{ A g}^{-1}$  ( $\approx 15.8 \text{ C}$ ,  $1 \text{ C} = 380 \text{ mA g}^{-1}$ ), the reversible capacity remains as high as  $374.6 \text{ mAh g}^{-1}$ . In addition, CC-Zn/K displays minimal capacity changes when the current density returns to  $0.1 \text{ A g}^{-1}$ , demonstrating favorable reversibility. These values are significantly higher than the cells with other carbon structures, confirming that microcrystalline and micropore configurations synergistically enhance Li-ion storage capacity and rate. Moreover, compared with the recently reported carbon materials, the CC-Zn/K still exhibits excellent rate performance (Figure 4c),<sup>[22,34–38]</sup> further confirming the superiority of the designed microcrystalline/microporous structure.

The Li-ion insertion mechanism was further analyzed for three different types of carbon structures, including high graphitization (graphite), low graphitization (CC), and microcrystalline/microporous (CC-Zn/K) carbons. As shown in the charging/discharging curves at a current density of  $0.2 \text{ A g}^{-1}$ , the ordered carbon lattice displays an evident Li-ion intercalated platform at a lower potential (0.1 V; Figure 4d), easily leading to sluggish Li-ion insertion kinetics and Li metal precipitation problem. While the distorted carbon lattice exhibits a sloping discharge platform (Figure 4e), indicating enhanced Li<sup>+</sup> intercalation kinetics through the modified diffusion pathways. For comparison, the microcrystal/microporous structure obtained via large-ions shuttle demonstrates a hybrid mechanism, featuring a pseudocapacitance adsorption process with a relatively large slope above 0.4 V and a Li-ion insertion platform with an average potential of 0.2 V (Figure 4e). The two behaviors can be respectively attributed to Li-ions adsorption in micropores and intercalation in microcrystals. Such carbon structural engineering enables enhanced Li storage capacity and accelerated diffusion kinetics, highlighting the significance of regulating the carbon lattice structure. Furthermore, the CC-Zn/K also exhibits favorable cycling performance. After 100 ( $0.2 \text{ A g}^{-1}$ , Figure 4g) and 1000 ( $2 \text{ A g}^{-1}$ , Figure 4h) cycles, it exhibits high reversible capacities of 1006 and  $400 \text{ mAh g}^{-1}$ , along with 98.2% and 97.3% capacity retention, respectively. The results confirm the stability of the designed microcrystal/micropores structure. Notably, the battery capacity in Figure 4g exhibits an initial decline followed by a recovery. This behavior originates from two competing processes: the SEI formation and electrode activation processes. The irretrievable consumption of Li-ion during SEI formation leads to an initial unsustainable "pseudo-high" capacity, and as the SEI evolution gradually stabilizes, the measured capacity gradually decreases. Concurrently, as the electrolyte progressively infiltrates the voids within the electrode, the Li-ion storage capacity gradually increases.

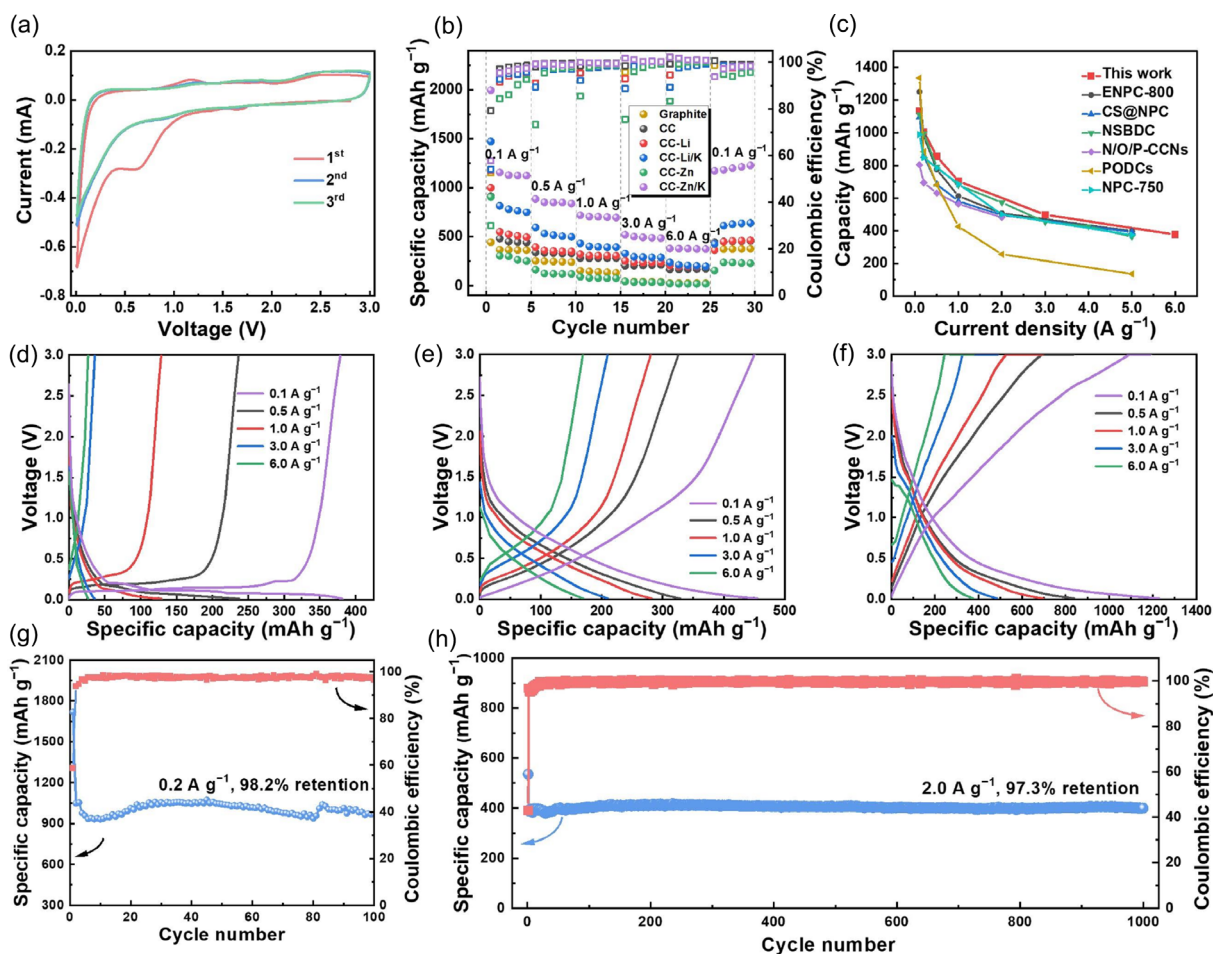


**Figure 4.** Electrochemistry performance tests. a) CV curves of CC-Zn/K at  $0.1 \text{ mV s}^{-1}$ ; b) rate performance of graphite, CC, and CC-Xs; c) comparison of the rate performance of CC-Zn/K and representative carbon materials; charging/discharging curves of d) graphite, e) CC, and f) CC-Zn/K; and cycle performance of CC-Zn/K tested at g)  $0.2 \text{ A g}^{-1}$  and h)  $2 \text{ A g}^{-1}$ .

To gain a deep understanding of the kinetics advantage of the microcrystal/micropores carbon, CV measurements were performed on graphite, CC, and CC-Zn/K at various scan rates ranging from  $0.2$  to  $2.0 \text{ mV s}^{-1}$ , as shown in Figure 5a, S9, Supporting Information. The relationship between the current ( $i$ ) and the scan rate ( $v$ ) can be described by the following equation

$$i = av^b \quad (1)$$

$$\log i = b \log v + \log a \quad (2)$$

where the exponent,  $b$ , can be determined from the slope of the logarithmic plot of  $i$  versus  $v$ . When  $b = 1.0$  indicates a capacitance-controlled process, while  $b = 0.5$  indicates a diffusion-controlled process.<sup>[39,40]</sup> The graphite with typical insertion reactions exhibits a smaller  $b$ -value of  $0.32/0.22$  (cathodic/anodic), while the  $b$ -value of amorphous-dominated CC is closer to  $1$  ( $0.79/0.86$ ). For comparison, the CC-Zn/K presents a medium  $b$ -value ( $0.76/0.63$ ), demonstrating a hybrid

mechanism of diffusion and capacitive behavior. The relative contributions of capacitance and diffusion were further analyzed using (Equation 3)

$$i(v) = k_1v + k_2v^{1/2} \quad (3)$$

In (Equation 3),  $i$  represents the current at a specific voltage, and  $v$  denotes the scan rate. The  $k_1v$  and  $k_2v^{1/2}$  indicate surface and diffusion control, respectively.<sup>[41,42]</sup> With increasing the scan rate, the capacitance contributions gradually increase because the capacitive behavior exhibits faster Li storage kinetics compared to diffusion-controlled processes (Figure 5d). Compared with graphite and CC, CC-Zn/K displays larger capacitance ratios that can reach 64% at a scan rate of  $2 \text{ mV s}^{-1}$  (blue area in Figure 5c). The dominant capacitive behavior can be attributed to the structure advantage of CC-Zn/K that the presence of numerous microporous structures and O/N active groups on edge enhances the double layers and Faraday capacitance. This, therefore, increases the Li storage capacity and kinetics of the CC-Zn/K.

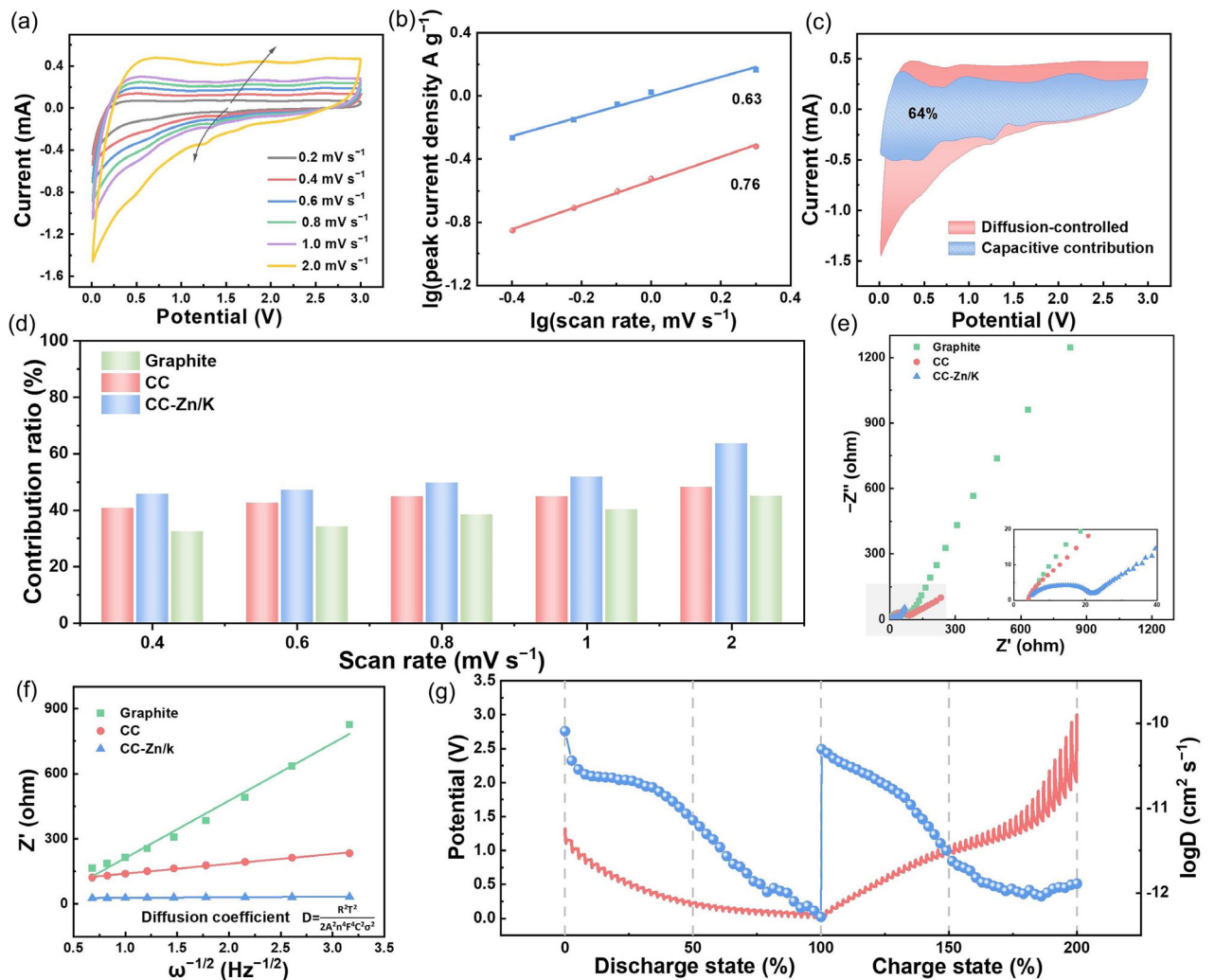


**Figure 5.** Reaction kinetics analysis. a) CV curves and b) b-value analysis of CC-Zn/K at scan rates ranging from 0.2 to 2.0 mV s<sup>-1</sup>; c) contribution ratio of capacitive and diffusion-controlled capacities of CC-Zn/K at 2.0 mV s<sup>-1</sup>; d) contribution ratio of capacitive capacities of CC, CC-Zn/K, and graphite at different scan rates; e) EIS and f) the relationship between  $Z'$  and  $\omega^{-1/2}$  at EIS low frequency of CC, CC-Zn/K, and graphite; g) GITT curves (red) and  $D_{Li^+}$  values (blue) during the lithiation and delithiation process of CC-Zn/K.

Electrochemical impedance spectroscopy (EIS) serves as an effective method for analyzing the kinetic behavior of the electrode. As shown in Figure 5e, the CC-Zn/K exhibits the smallest semicircle diameter in the high-frequency region, confirming a significantly reduced charge transfer resistance ( $R_{ct}$ ) when compared with the regular graphite crystal and amorphous-dominated CC. Additionally, the slope of the straight line under the low-frequency region reflects the Li-ion diffusion ability in the material and is inversely proportional to the Warburg diffusion resistance ( $W$ ).<sup>[43]</sup> According to the fitting curves between  $Z'$  and  $\omega^{-1/2}$ , graphite displays the largest  $W$  coefficient ( $\sigma$ ) value (Figure 5f), indicating the slow diffusion kinetics of Li-ions within the closely packed lattice. For comparison, the CC-Zn/K exhibits the smallest  $\sigma$  value, further confirming that micro-crystalline structure facilitates a rapid Li-ion transfer rate. To further assess the diffusion coefficient of  $Li^+$  ( $D_{Li^+}$ ) in the three electrodes, the galvanostatic intermittent titration technique (GITT) was employed. The measurements were

performed at a pulse current of 0.1 A g<sup>-1</sup> for 10 min, with a subsequent rest interval of 1 h (Figure S 10, Supporting Information). The relevant diffusion coefficients of  $Li^+$  were determined by employing Fick's second law, which is expressed by the following formula

$$D = \frac{4L^2}{\pi\tau} \left( \frac{\Delta E_s}{\Delta E_t} \right)^2 \quad (4)$$

in which,  $\tau$  (s) represents the pulse duration, and  $L$  (cm) represents the Li-ion diffusion length which is simplified to the thickness of the electrodes.<sup>[44]</sup> Additionally,  $\Delta E_s$  and  $\Delta E_t$  represents the potential change caused by the pulse and during the constant current charging/discharging process, respectively. Figure 5g shows the  $D_{Li^+}$  of lithiation/delithiation process. During the Li insertion process (discharging), the calculated  $D_{Li^+}$  values maintain a high value in the high-potential region and then decrease.

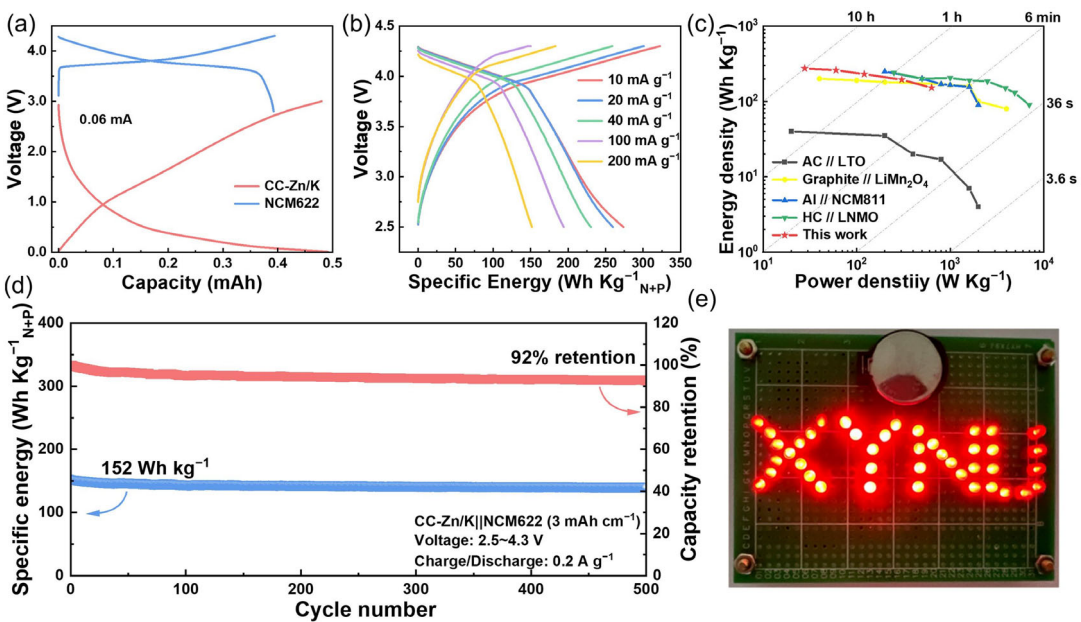


**Figure 6.** The charge–discharge profiles of a) CC-Zn/K anode and NCM622 cathode, as well as b) the CC-Zn/K||NCM622 full cell with specific energy calculation based on the mass of cathode and anode; c) Ragone plots of different energy storage devices; d) cycle performance of the CC-Zn/K||NCM622 full cell; and e) digital photos of a coin full cell lighting LEDs.

Additionally, the  $D_{\text{Li}^+}$  values also show declines during the Li extraction stage (charging). This decrease could be attributed to the reduction of Li-ion concentration in the electrode material.<sup>[44,45]</sup> The average diffusivity coefficient of the CC-Zn/K is  $10^{-12}\text{--}10^{-10}$  cm<sup>2</sup> s<sup>-1</sup>, which is higher than those of CC ( $10^{-13}\text{--}10^{-11}$ , Figure S11, Supporting Information) and graphite ( $10^{-15}\text{--}10^{-10}$ , Figure S12, Supporting Information). These results confirm that the regulated microcrystalline structure can effectively shorten the Li-ion diffusion path, thus exhibiting better electrochemical performance.

To evaluate the practical applicability of the CC-Zn/K with abundant microcrystals and micropores, full batteries were constructed using the CC-Zn/K as the anode and LiNi<sub>0.8</sub>Co<sub>0.2</sub>Mn<sub>2</sub> (NCM622) as the cathode. For optimal energy and power density, the full cell was operated within a voltage range of 2.5–4.3 V, and the ratio of negative/positive (N/P) capacities was 1.2 (Figure 6a, S13, Supporting Information). During the galvanostatic charge–discharge (GCD) test, current and energy densities were calculated based on the total mass of both the anode and cathode. As shown in Figure 6b, the full cell shows an energy density of 275 Wh kg<sup>-1</sup>, accompanied by a power density of 28 W kg<sup>-1</sup> (at 0.01 A g<sup>-1</sup>). Notably, with increasing power densities, the energy density still remains 152 at 633 W kg<sup>-1</sup> (Figure 6c). Compared to previously reported carbon-based batteries, the Ragone plots of CC-Zn/K||NCM622 full cell show a superior relationship between its energy and power density.<sup>[45–48]</sup> Furthermore, the full cell exhibits outstanding cycling stability due to the rapid reaction kinetics of the microcrystalline carbon anode (Figure 6d). A notable capacity retention of 92% can be achieved after 500 cycles at 0.2 A g<sup>-1</sup>, attributed to the rapid reaction kinetics and favorable structural maintenance of the CC-Zn/K anode. In addition, the assembled CC-Zn/K||NCM622 cell was able to power a group of LED lights

(Figure 6e), confirming the practical applicability of the microcrystalline carbon architecture.

### 3. Conclusion

In summary, we proposed an effective strategy to enable carbon crystalline structure regulation by introducing cationic molten salts during the carbonization process. Systematic investigations reveal that the cation shuttling within the carbon framework can effectively inhibit the graphitization while simultaneously optimizing carbon microstructure. Remarkably, Zn and K ions exhibit the functionalities of promoting the evolution of carbon microcrystals and the generation of micropores, respectively. The modulated microcrystalline carbon significantly improved the Li intercalation kinetics and storage mechanism, thus resulting in an ultrahigh reversible capacity (up to 1156 mAh g<sup>-1</sup> at 0.1 A g<sup>-1</sup>), excellent rate capability (374.6 mAh g<sup>-1</sup> at 6 A g<sup>-1</sup>), as well as outstanding cycling stability (97.3% capacity retention after 1000 cycles at 2 A g<sup>-1</sup>). Notably, the assembled NCM622-based full batteries demonstrated favorable fast charging ability along with 92% capacity retention over 500 cycles at 0.2 A g<sup>-1</sup>. These findings highlight the significant impact of carbon crystal engineering on enhancing battery performance and demonstrate an effective strategy for developing a high-performance Li-ion battery anode.

### 4. Experimental Section

#### Materials Preparation

The fabrication of coal-based porous carbon involved a straightforward approach utilizing a ZnCl<sub>2</sub>/KCl molten salt system (with a

mol ratio of 49:51 for  $\text{ZnCl}_2$  to  $\text{KCl}$  and a melting point of  $230^\circ\text{C}$ ). In this process, the coal and  $\text{ZnCl}_2/\text{KCl}$  molten salt system were thoroughly mixed through mechanical grinding. Subsequently, the mixture underwent high-temperature carbonization treatment under an Ar atmosphere, resulting in the formation of coal-based porous carbon. These carbon samples were designated as CC-Zn/K-T, where  $T$  denotes the carbonization temperature,  $T = 600, 700, 800, 1000$ , and  $1400^\circ\text{C}$ . The experimental method for the preparation of coal-based porous carbon from other molten salts is the same as that for CC-Zn/K. The mass ratio of coal to molten salt ( $\text{LiCl}$ ,  $\text{LiCl}/\text{KCl}$ , and  $\text{ZnCl}_2$ ) is 1:10, where the molten salt  $\text{LiCl}/\text{KCl}$  is 9:11 by mass (with a melting point of  $353^\circ\text{C}$ ). Finally, the above samples were cleaned with hydrochloric acid (HCl), deionized water, and dried at  $80^\circ\text{C}$  for 12 h.

## Materials Characterization

Phase compositions of the products were characterized by XRD (Bruker D8) with  $\text{Cu K}\alpha$  radiation ( $\lambda = 0.15406 \text{ nm}$ ). XPS was collected by using a Thermo ESCALAB 250 instrument with a monochromated Al X-ray source at 1486.6 eV. Raman spectroscopy was taken on Bruker R200-L. Morphologies of samples were studied by using a scanning electron microscope (Hitachi S-4800) and a TEM (Hitachi H-600). Nitrogen adsorption–desorption isotherms were recorded by an ASAP Pressure Sorption Analyzer (Micromeritics Shanghai).

## Electrochemical Tests

A slurry was obtained by mixing the samples, acetylene black, and polyvinylidene fluoride in N-methyl-2-pyrrolidone with a mass ratio of 8:1:1, which was uniformly spread onto a Cu foil. Then, it was dried at  $110^\circ\text{C}$  overnight in a vacuum oven. Cells were assembled in an argon-filled glove box with the lithium metal as the counter electrode, Celgard 2400 membrane as the separator, and  $\text{LiPF}_6$  (1 M) in mixed solvents of ethyl carbonate/diethyl carbonate (1:1, v/v) as the electrolyte. CV was conducted on a CHI 660D working station. GCD measurements were carried out with a Land (CT2001A, China) at 0.01–3.00 V. The GITT was conducted to detect the diffusion kinetics of the electrode, in which the cells were delithiated/lithiated at 0.01–3.00 V at  $0.1 \text{ A g}^{-1}$ , and the pulse current time and rest time were 10 and 60 min, respectively. EIS measurements were conducted by the VMP-30 working station, and interrogated across a sweeping frequency range from 10 kHz down to 10 mHz.

## Acknowledgements

F.M. and X.K. contributed equally to this work. This work was supported by Natural Science Foundation of Henan Province (grant nos. 242300420001 and 232300420387), Frontier Exploration Projects of Longmen Laboratory (grant no. LMQYTSKT021), the National Natural Science Foundation of China (grant nos. 52201283 and 22208273), China Postdoctoral Science Foundation (grant nos. 2022TQ0291 and 2022M712869), the Nanhua Scholars Program for Young Scholars of XYNU, and the Analysis Testing Center of Xinyang Normal University.

## Conflict of Interest

The authors declare no conflict of interest.

## Data Availability Statement

Research data are not shared.

## Keywords:

anode · carbon · Li-ion batteries · microcrystal

- [1] J. Xie, Y.-C. Lu, *Nat. Commun.* **2020**, *11*, 2499.
- [2] R. Wang, L. Wang, R. Liu, X. Li, Y. Wu, F. Ran, *ACS Nano* **2024**, *18*, 2611.
- [3] M. Li, J. Lu, Z. Chen, K. Amine, *Adv. Mater.* **2018**, *30*, 1800561.
- [4] H. J. Kwon, J.-Y. Hwang, H.-J. Shin, M.-G. Jeong, K. Y. Chung, Y.-K. Sun, H.-G. Jung, *Nano Lett.* **2020**, *20*, 625.
- [5] F. Duffner, N. Kronemeyer, J. Tübke, J. Leker, M. Winter, R. Schmuck, *Nat. Energy* **2021**, *6*, 123.
- [6] G. Harper, R. Sommerville, E. Kendrick, L. Driscoll, P. Slater, R. Stolk, A. Walton, P. Christensen, O. Heidrich, S. Lambert, A. Abbott, K. Ryder, L. Gaines, P. Anderson, *Nature* **2019**, *575*, 75.
- [7] P. Cui, H. Wang, B. Yang, S. Dong, M. Jiao, R. Zhao, K. Zhu, Y.-Z. Fang, Z. Zhou, D. Cao, *Batteries Supercaps* **2024**, *7*, e202400274.
- [8] A. Bhandari, C. Peng, J. Dziedzic, J. R. Owen, D. Kramer, C.-K. Skylaris, *J. Mater. Chem. A* **2022**, *10*, 11426.
- [9] C. Sun, X. Ji, S. Weng, R. Li, X. Huang, C. Zhu, X. Xiao, T. Deng, L. Fan, L. Chen, X. Wang, C. Wang, X. Fan, *Adv. Mater.* **2022**, *34*, 2206020.
- [10] J. Wang, D. Yu, X. Sun, H. Wang, J. Li, *eScience* **2024**, *4*, 100252.
- [11] D. Xia, E. P. Kamphaus, A. Hu, S. Hwang, L. Tao, S. Sainio, D. Nordlund, Y. Fu, H. Huang, L. Cheng, F. Lin, *ACS Energy Lett.* **2023**, *8*, 1379.
- [12] F. Zhang, X. Liu, M. Yang, X. Cao, X. Huang, Y. Tian, F. Zhang, H. Li, *Nano Energy* **2020**, *69*, 104443.
- [13] X. Dou, I. Hasa, D. Saurel, C. Vaalma, L. Wu, D. Buchholz, D. Bresser, S. Komaba, S. Passerini, *Mater. Today* **2019**, *23*, 87.
- [14] L. Kalder, M. Härmä, J. Aruväli, E. Lust, E. Hark, *ECS Meeting Abstracts* **2023**, MA2023-01, 816.
- [15] L. Qin, S. Xu, Z. Lu, L. Wang, L. Chen, D. Zhang, J. Tian, T. Wei, J. Chen, C. Guo, *Diamond Relat. Mater.* **2023**, *136*, 110065.
- [16] Y. Huang, X. Hu, Y. Li, X. Zhong, Z. He, Z. Geng, S. Gan, W. Deng, G. Zou, H. Hou, X. Ji, *Adv. Funct. Mater.* **2024**, *34*, 2403648.
- [17] T. Wang, R. Li, Q. Liu, W. Liu, *Recent Pat. Nanotechnol.* **2025**, *19*, 257.
- [18] C. Bao, Z. Liu, Z. Yang, L. Shi, C. He, H. Chen, Y. He, Q. Liu, L. Yang, H. Liu, *Electrochim. Acta* **2023**, *463*, 142821.
- [19] G. Wang, A. Mijailovic, J. Yang, J. Xiong, S. E. Beasley, K. Mathew, B. Zhou, W. Lu, B. W. Sheldon, Q. Wu, *J. Mater. Chem. A* **2023**, *11*, 21793.
- [20] J. Baek, H.-M. Lee, J.-S. Roh, H.-S. Lee, H. S. Kang, B.-J. Kim, *Microporous Mesoporous Mater.* **2016**, *219*, 258.
- [21] X. Zhao, H. Chen, F. Kong, Y. Zhang, S. Wang, S. Liu, L. A. Lucia, P. Fatehi, H. Pang, *Chem. Eng. J.* **2019**, *364*, 226.
- [22] C. Xu, G. Ma, W. Yang, Y. Wang, Y. Jia, Y. Sun, X. Kong, J. Yang, H. Liu, X. Zhang, G. Huang, Y. Li, *J. Energy Storage* **2023**, *65*, 107256.
- [23] G. Lee, K. B. Min, M. E. Lee, Y.-K. Lee, H. R. Lee, S.-S. Kim, S. Y. Cho, H.-I. Joh, Y.-K. Kim, S. Lee, *Chem. Eng. J.* **2024**, *479*, 147766.
- [24] P. Ouzilleau, A. E. Gheribi, P. Chartrand, G. Soucy, M. Monthoux, *Carbon* **2019**, *149*, 419.
- [25] N. Yang, L. Ji, H. Fu, Y. Shen, M. Wang, J. Liu, L. Chang, Y. Lv, *Chin. Chem. Lett.* **2022**, *33*, 3961.
- [26] J. Meng, X. Liu, J. Li, Q. Li, C. Zhao, L. Xu, X. Wang, F. Liu, W. Yang, X. Xu, Z. Liu, C. Niu, L. Mai, *Nano Lett.* **2017**, *17*, 7773.
- [27] W. Lin, S. Zhao, B. Lu, F. Jiang, Z. Lu, Z. Xu, *Energy Mater.* **2024**, *4*, 400078.
- [28] H. Li, X. He, T. Wu, B. Jin, L. Yang, J. Qiu, *Fuel Process. Technol.* **2022**, *230*, 107203.
- [29] Y. Dong, S. Zhang, X. Du, S. Hong, S. Zhao, Y. Chen, X. Chen, H. Song, *Adv. Funct. Mater.* **2019**, *29*, 1901127.
- [30] W. Xie, S. He, S. Fang, D. Zhou, Y. Zhang, L. Liang, L. Wang, D. Wang, *Nano Express* **2021**, *2*, 010001.
- [31] K. Ning, G. Zhao, H. Liu, M. Hu, F. Huang, H. Li, L. Zhang, G. Zhu, H. Wang, J. Shi, *Diamond Relat. Mater.* **2022**, *126*, 109080.
- [32] X. Wang, Y. Gao, J. Ma, J. Guo, Y. Zeng, M. Wu, *Sol. Energy Mater. Sol. Cells* **2024**, *266*, 112687.
- [33] K. Shang, Y. Liu, P. Cai, K. Li, Z. Wen, *J. Mater. Chem. A* **2022**, *10*, 6489.
- [34] H. Liang, H. Zeng, B. Xing, L. Feng, Z. Chen, H. Guo, B. Xu, X. Qu, C. Zhang, R. Li, *J. Alloys Compd.* **2023**, *968*, 172015.
- [35] T. Yang, J. Zhong, J. Liu, Y. Yuan, D. Yang, Q. Mao, X. Li, Z. Guo, *Adv. Funct. Mater.* **2021**, *31*, 2009433.

- [36] B. Wang, Y. Wang, Y. Peng, X. Wang, J. Wang, J. Zhao, *J. Power Sources* **2018**, *390*, 186.
- [37] W. Yang, W. Lu, W. Wang, *Energy Fuels* **2022**, *36*, 669.
- [38] T. Wang, J. Sha, W. Wang, Y. Ji, Z.-M. Zhang, *Chin. Chem. Lett.* **2023**, *34*, 107929.
- [39] H. Chen, N. Sun, Q. Zhu, R. A. Soomro, B. Xu, *Adv. Sci.* **2022**, *9*, 2200023.
- [40] X. Pu, D. Zhao, C. Fu, Z. Chen, S. Cao, C. Wang, Y. Cao, *Angew. Chem., Int. Ed.* **2021**, *60*, 21310.
- [41] D. Chao, C. Zhu, P. Yang, X. Xia, J. Liu, J. Wang, X. Fan, S. V. Savilov, J. Lin, H. J. Fan, Z. X. Shen, *Nat. Commun.* **2016**, *7*, 12122.
- [42] D. Chao, P. Liang, Z. Chen, L. Bai, H. Shen, X. Liu, X. Xia, Y. Zhao, S. V. Savilov, J. Lin, Z. X. Shen, *ACS Nano* **2016**, *10*, 10211.
- [43] M. Oldenburger, B. Bedürftig, A. Gruhle, F. Grimsmann, E. Richter, R. Findeisen, A. Hintennach, *J. Energy Storage* **2019**, *21*, 272.
- [44] J. H. Park, H. Yoon, Y. Cho, C.-Y. Yoo, *Materials* **2021**, *14*, 4683.
- [45] B. Ji, F. Zhang, M. Sheng, X. Tong, Y. Tang, *Adv. Mater.* **2017**, *29*, 1604219.
- [46] H. Yu, X. Dong, Y. Pang, Y. Wang, Y. Xia, *Electrochim. Acta* **2017**, *228*, 251.
- [47] S. Dsoke, B. Fuchs, E. Gucciardi, M. Wohlfahrt-Mehrens, *J. Power Sources* **2015**, *282*, 385.
- [48] W. A. Appiah, J. Park, L. Van Khue, Y. Lee, J. Choi, M.-H. Ryou, Y. M. Lee, *Electrochim. Acta* **2016**, *187*, 422.

Manuscript received: May 15, 2025

Revised manuscript received: July 28, 2025

Version of record online: